

ARTICLE OPEN

Ultrafast optically induced ferromagnetic/anti-ferromagnetic phase transition in GdTiO_3 from first principlesGuru Khalsa¹ and Nicole A. Benedek¹

Epitaxial strain and chemical substitution have been the workhorses of functional materials design. These static techniques have shown immense success in controlling properties in complex oxides through the tuning of subtle structural distortions. Recently, an approach based on the excitation of an infrared active phonon with intense midinfrared light has created an opportunity for dynamical control of structure through special nonlinear coupling to Raman phonons. We use first-principles techniques to show that this approach can dynamically induce a magnetic phase transition from the ferromagnetic ground state to a hidden antiferromagnetic phase in the rare earth titanate GdTiO_3 for realistic experimental parameters. We show that a combination of a Jahn–Teller distortion, Gd displacement, and infrared phonon motion dominate this phase transition with little effect from the octahedral rotations, contrary to conventional wisdom.

npj Quantum Materials (2018)3:15 ; doi:10.1038/s41535-018-0086-3

INTRODUCTION

The properties of ABO_3 perovskites arise not only from the crystal structure generally, they also depend sensitively on small structural distortions, in contrast with most other inorganic materials families. For example, the magnetoresistive properties of perovskite manganites,¹ and metal–insulator transitions in the perovskite nickelate^{2–4} and titanate families^{5,6} are strongly linked with so-called ‘rotations’ of the BO_6 octahedra, which are associated with zone-boundary phonons of the cubic perovskite structure. Researchers have learned how to successfully tune this dependence using a variety of techniques, such as epitaxial strain^{7,8} and stabilization,⁹ pressure,¹⁰ and doping.¹ Dynamical control of the properties of perovskites has been far more challenging, and has so far been largely based on light-induced electronic excitation or temperature changes.^{11–13}

Recent experiments have demonstrated the potential for modifying the properties of materials using ultrafast optical pulses to selectively and coherently excite particular phonon modes. One such mechanism involves optical excitation of an infrared (IR)-active phonon Q_{IR} , which produces a displacement of a Raman-active mode Q_{R} due to a particular anharmonic coupling between the modes of the form $Q_{\text{IR}}^2 Q_{\text{R}}$ (although the relevant coupling term is not always clear in experimental studies, most theoretical works so far have focused on couplings of the form $Q_{\text{IR}}^2 Q_{\text{R}}$). This nonlinear phononic effect, and the subtle structural changes it induces, has been invoked to interpret observations of a five-orders-of-magnitude decrease in resistivity in $\text{Pr}_{0.7}\text{Ca}_{0.3}\text{MnO}_3$,^{14,15} a material that is insulating at equilibrium at all measured temperatures.^{16,17} Additionally, the charge- and orbitally ordered phase of $\text{La}_{1/2}\text{Sr}_{3/2}\text{MnO}_4$ can be destabilized well below the orbital ordering temperature by selective vibrational excitation of an Mn–O stretching mode.¹⁸ In a particularly notable example, the observation of transient superconductivity above the transition temperature in vibrationally excited $\text{YBa}_2\text{Cu}_3\text{O}_{6.5}$ was also attributed to a nonlinear phononic effect.¹⁹ Experiments that

exploit this mechanism have, together with first-principles calculations,^{15,20–22} produced profound new insights into the structural dynamics of materials out of equilibrium.

Here, we use the family of orthorhombic perovskite titanates to develop a generalized theory of nonlinear phononics, which we use in combination with density functional theory calculations to reveal the existence of a hidden magnetic phase in GdTiO_3 accessible under experimentally realistic conditions (Fig. 1). It is generally understood that rotations of the TiO_6 octahedra strongly affect the coupling between neighboring $\text{Ti}-t_{2g}$ orbitals and therefore control the bandwidth and magnetic superexchange interactions. In the equilibrium phase diagram, the rotation amplitudes increase as the size of the rare earth cation decreases. This change in rotation amplitudes is accompanied by a change in the magnetic ground state, with G-AFM SmTiO_3 and FM GdTiO_3 straddling the boundary between the AFM and FM parts of the phase diagram. Interestingly, an A-type AFM phase has been speculated to exist between SmTiO_3 and GdTiO_3 ; however, no stoichiometric system exists between these materials. Although it may seem that the A-AFM phase could be obtained by judiciously tuning octahedral rotation angles, Mochizuki and Imada⁵ point out that the Jahn–Teller mode plays a critical role in stabilizing the A-AFM phase (Pavarini et al.²³ had a similar insight). In particular, the A-AFM phase requires the combination of a “strong” Jahn–Teller distortion (as in GdTiO_3) and “moderate” octahedral rotation distortion (as in SmTiO_3). However, the Jahn–Teller distortion is coupled to the rotations and weakens rapidly as the rotations decrease. There is no known way to independently control the relative magnitudes of these distortions. Indeed, as far as we are aware, neither bulk chemical techniques (solid solutions) nor strain engineering have been able to experimentally stabilize the A-AFM phase in any perovskite titanate.

We demonstrate that the nonlinear phononics mechanism can be used to essentially “switch off” the net magnetization in GdTiO_3 by inducing an A-AFM phase. Although we find that the A-AFM

¹Department of Materials Science and Engineering, Cornell University, Ithaca, NY 14853, USA

Correspondence: Guru Khalsa (guru.khalsa@cornell.edu) or Nicole A. Benedek (nbenedek@cornell.edu)

Received: 20 December 2017 Revised: 8 February 2018 Accepted: 9 February 2018

Published online: 12 March 2018

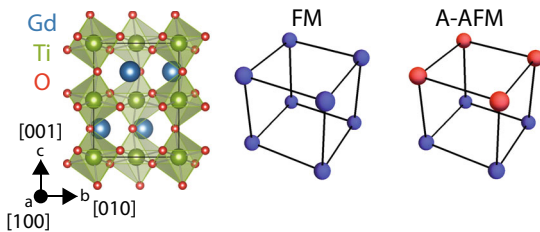


Fig. 1 Crystal and magnetic structures of GdTiO_3 . Orthorhombic structure of GdTiO_3 in the $Pbnm$ setting and schematic showing ferromagnetic (FM) and A-type antiferromagnetic (A-AFM) magnetic configurations for the Ti 3d¹ spins. The red and blue spheres correspond to different spin directions

phase can be realized dynamically in bulk GdTiO_3 , the required peak electric fields are quite high. However, we show that a modest amount of epitaxial strain can position GdTiO_3 closer to the phase boundary, such that the A-AFM phase is induced at low peak electric fields of the optical pulse. We also elucidate the origin of the magnetic transition in terms of the structural distortions that accompany the optical excitation. Surprisingly, although the octahedral rotation distortions are affected by optical excitation, their amplitudes change very little from their equilibrium values and their effect on the magnetic configuration energy is negligible. Instead, we find that it is primarily the Jahn-Teller mode that plays the key role in switching off the net magnetization in GdTiO_3 , and dynamically inducing the A-AFM phase. These are precisely the conditions under which Mochizuki and Imada speculated that the A-AFM phase could be realized. Our results demonstrate that the nonlinear phononics mechanism can be leveraged to modulate the complex interplay between structural distortions in perovskites, and their electronic and magnetic properties. We also shed light on the structural dynamics of perovskites out of equilibrium, a regime in which these materials have been little explored.

RESULTS

Theory

Two-mode model. An expansion of the lattice energy clarifies the nonlinear phononics process for a centrosymmetric crystal in which the IR and Raman modes have different symmetry. For simplicity we first consider a model involving only a single IR mode and a single Raman mode (this model is similar to that presented in refs. ^{15,24}). The lattice energy U is defined by

$$U = \frac{1}{2} \omega_{\text{IR(R)}}^2 Q_{\text{IR(R)}}^2 + \frac{1}{2} \omega_{\text{R}}^2 Q_{\text{R}}^2 + A Q_{\text{IR}}^2 Q_{\text{R}} + \Delta \vec{P} \cdot \vec{E}(t), \quad (1)$$

where $\omega_{\text{IR(R)}}$ and $Q_{\text{IR(R)}}$ are, respectively, the frequency and amplitude of the IR (Raman) phonon and A is a coupling coefficient. The last term contains the polarization change in the crystal, defined as $\Delta \vec{P} = \tilde{Z}^* Q_{\text{IR}}$, where \tilde{Z}^* , known as the mode effective charge,²⁵ describes the strength of the coupling between the excited IR phonon and the electric field of the light pulse (\vec{E}) (we ignore the effects of the oscillating IR mode on the polarization). Note that since Q_{R}^2 is invariant under all symmetry operations of the crystal, in order for A to be non-zero, Q_{R} must also be invariant under all symmetry operations of the crystal. By convention, we label this totally symmetric mode A_g . Nonlinear coupling of the form $Q_{\text{IR}} Q_{\text{R}}^2$, linear in the IR mode displacement and quadratic in Raman mode displacement, are not allowed because of inversion symmetry (taking $Q_{\text{IR}} \rightarrow -Q_{\text{IR}}$). In noncentrosymmetric crystals, some IR phonons are fully symmetric. In this case, these terms are allowed.

We desire a large, static displacement of the Raman mode that is long-lived on the timescale of the IR mode. Taking derivatives of Eq. (1) with respect to the IR and Raman amplitudes for a fixed

electric field direction,

$$\ddot{Q}_{\text{IR}} = -\omega_{\text{IR}}^2 Q_{\text{IR}} - 2A Q_{\text{IR}} Q_{\text{R}} - \tilde{Z}^* E(t), \quad (2)$$

$$\ddot{Q}_{\text{R}} = -\omega_{\text{R}}^2 Q_{\text{R}} - A Q_{\text{IR}}^2, \quad (3)$$

reveals that this depends on three materials-specific criteria: (1) strong coupling between the excited IR mode and the incoming light pulse (large \tilde{Z}^* ²⁶), (2) strong coupling between the excited IR mode and the Raman mode (large A), and (3) the frequency of the IR phonon should be higher than that of the Raman mode, such that the Raman mode does not oscillate within the period of the IR mode. Equation (3) also shows that as long as the IR phonon is ringing, there will be a unidirectional force on the Raman mode.

Equations (1)–(3) provide useful insight into the basic physical process exploited in the nonlinear phononics mechanism; however, real materials contain many IR and Raman phonons. In general, when an IR mode is optically excited, all symmetry-allowed modes will contribute to the dynamical response. The two-mode model ignores the dynamic coupling between Raman modes and will provide a poor description of the structural dynamics when the coupling between these modes is strong. Additional complications arise when more than one IR mode is excited by the incoming light pulse, as shown in Fig. 2. As the oscillator strength of the second mode increases, the structural dynamics becomes increasingly complicated, and the two-mode model will again fail to provide a correct description. Ultimately, without knowing the relevant nonlinear coupling coefficients explicitly, it is not possible to predict a priori which modes will be strongly coupled or have a large contribution to the dynamical response. Hence, all IR and Raman phonons should be treated on equal footing. We present a model below that does just that.

Many-mode model. In order to make the problem concrete and tractable, here we focus on the case where light is polarized along the principal crystallographic axes and parallel with the particular IR phonon we wish to excite. Additionally, we use the perovskite $Pbnm$ crystal structure as a starting point, without loss of generality, because it is the most stable crystal structure for more than half of all perovskites, including GdTiO_3 (extension of this model to arbitrary crystal systems—with or without inversion symmetry—is straightforward, but cumbersome).

The orthorhombic $Pbnm$ structure has 20 atoms per primitive cell and therefore 60 zone-centered phonons. There are 25 IR-active phonons: 9 polarized along each of the a - and b -axes ([100] and [010]), and 7 polarized along the c -axis ([001]). Additionally, there are seven Raman-active phonons of A_g symmetry that are accessible through the nonlinear phononics process. Expanded to

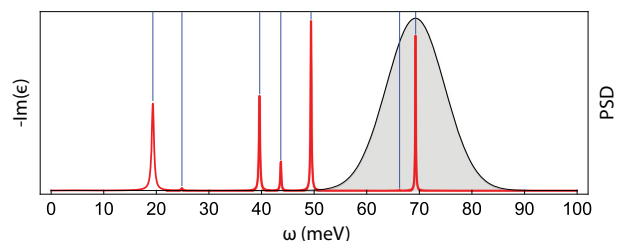


Fig. 2 Simultaneous excitation of multiple IR modes. Schematic of the imaginary part of the dielectric function (left axis) with superimposed 300 fs Gaussian pulse (right axis, power spectral density). The horizontal blue lines highlight the positions of the IR modes, which are all polarized along the same crystallographic axis. Even though the pulse is tuned to be resonant with a particular IR mode, because the pulse has a finite width, it will also excite other IR modes that are close in frequency to the target phonon

third order, Eq. (1) becomes

$$U = \frac{1}{2} \sum_i \omega_i^2 Q_i^2 + \frac{1}{2} \sum_a \omega_a^2 Q_a^2 + \sum_{ia} A_{ia} Q_i^2 Q_a + \sum_{ija} B_{ija} Q_i Q_j Q_a + \sum_{\alpha\beta\gamma} C_{\alpha\beta\gamma} Q_\alpha Q_\beta Q_\gamma + \Delta \vec{P} \cdot \vec{E}(t). \quad (4)$$

We use Latin indices (i, j, \dots) for IR-active phonons and Greek indices (α, β, \dots) for Raman-active phonons. Again, A_{ia} leads to a unidirectional displacement of mode a but now multiple Raman modes may be displaced by selective excitation of IR mode i . The B_{ija} terms allow for coupling between two different IR modes and a Raman mode. Juraschek et al.²² explored this coupling term theoretically for the case of two IR phonons polarized along different directions, where a coupling to non- A_g Raman phonons is induced. Nova et al.²⁷ have explored this term experimentally by simultaneously exciting two IR phonons with different polarizations in ErFeO₃. This term also couples two IR phonons with parallel polarization, again displacing an A_g Raman mode. The $C_{\alpha\beta\gamma}$ term couples three displaced Raman modes. Since multiple IR modes are now included the change in the polarization must also be expanded as $\Delta \vec{P} = \sum_i \tilde{Z}_i^* Q_i$.

Taking derivatives of Eq. (4) gives the equations of motion for the nonlinear phononics process to third order:

$$\ddot{Q}_i = -\omega_i^2 Q_{iR} - 2 \sum_a A_{ia} Q_i Q_a - 2 \sum_{ja} B_{ija} Q_j Q_a - \tilde{Z}_i^* E(t), \quad (5)$$

$$\ddot{Q}_a = -\omega_a^2 Q_a - \sum_i A_{ia} Q_i^2 - \sum_{ij} B_{ija} Q_i Q_j - 3 \sum_{\beta\gamma} C_{\alpha\beta\gamma} Q_\beta Q_\gamma. \quad (6)$$

We describe below how we integrate the many-mode model with density functional theory calculations to obtain a first-principles description of the structural dynamical response of a given material to optical excitation.

Integrating the many-mode model with first-principles calculations. Figure 3 shows the workflow we have implemented for obtaining the required inputs to the many-mode model, and for exploring the dynamical response of materials induced through the nonlinear phononics mechanism. A number of different steps are involved:

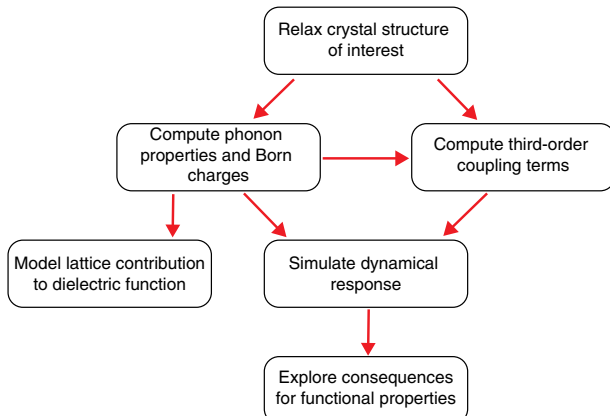


Fig. 3 Practical implementation of many-mode model. Workflow illustrating the calculations required and steps involved in simulating the dynamical response of a material to optical excitation using the many-mode model

- Relax the crystal structure of interest: The atomic positions and lattice parameters of the given material are fully relaxed using density functional theory. Forces must be tightly converged to ensure phonon properties are accurate.
- Compute phonon properties and Born charges: Phonon frequencies, eigenvectors, and Born effective charges are calculated using density functional perturbation theory. The eigenvectors and Born charges are required for calculation of the mode effective charges, which appear in Eqs. (5) and (6), along with the phonon frequencies.
- Model lattice contribution to the dielectric function: The phonon properties and Born charges are also used to model the lattice dielectric function. This is not strictly required for simulating the dynamical response; however, it is helpful for connecting our model with experimental information, such as the reflectivity and zero-frequency dielectric response.
- Compute third-order coupling terms: The third-order nonlinear coupling coefficients A_{ia} , B_{ija} , and $C_{\alpha\beta\gamma}$ are calculated with density functional theory using finite differences. Details are provided in the Methods section.
- Simulate dynamical response: A particular IR mode is selected for optical excitation, and the dynamical response of the crystal is simulated by numerically solving Eqs. (5) and (6). The optical pulse characteristics (timescale, shape, and peak electric field) are described in the Methods section.
- Explore consequences for functional properties: The many-mode model outputs a set of IR and Raman amplitudes, which are added back to the relaxed crystal structure to give a snapshot of the dynamical response of the material to optical excitation. The consequences for the band gap, magnetic configurations, and other properties can then be explored using density functional theory.

Magnetic phase transition in GdTiO₃

GdTiO₃ adopts the distorted *Pbnm* crystal structure with a ferromagnetic alignment of the Ti 3d¹ spins below \sim 30 K. As mentioned above, GdTiO₃ contains a number of IR-active modes and we found it was possible to position the system both closer to and further away from the FM-A-AFM phase boundary, depending on which mode we chose to excite. We compared the magnetic configuration energy of the A-AFM, G-AFM, and C-AFM states with the FM state for excitation of various IR modes and identified a 72.4 meV phonon polarized along the crystallographic *c*-axis ([001] direction) as being most likely to induce the desired magnetic phase transition. For all the results presented below, we checked that the material remains insulating. Figure 4 shows the

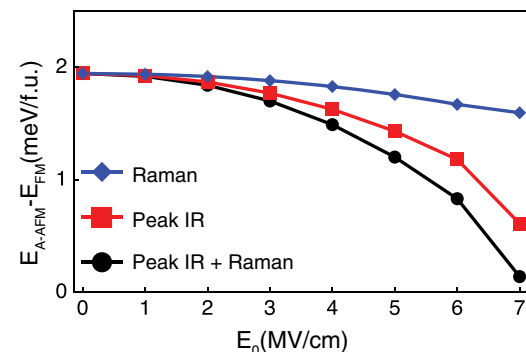


Fig. 4 Phonon-induced change in magnetism in bulk GdTiO₃. Simulated energy difference between the A-AFM and FM phases as a function of peak electric field for 72.4 meV, [001] polarized, IR phonon. A positive energy difference indicates that the FM phase is more stable than A-AFM

difference in the magnetic configuration energy between the FM and A-AFM states as a function of peak electric field (we also checked the energy difference between the FM phase and the other AFM orders but the A-AFM phase remains closest in energy to FM over the entire peak electric field range). The optically induced change in magnetic energy results from both the oscillating IR phonons (due to a biquadratic spin-phonon coupling) and the unidirectionally displaced Raman phonons. This is most clearly understood by expanding the out-of-plane (c -axis) Heisenberg exchange constant, J_c , in both the oscillating excited mode $Q_{\text{IR},0}$ and the total unidirectionally displaced Raman mode amplitudes $Q_{\text{R},0}$. By symmetry alone, $J_c \rightarrow J_c(1 + aQ_{\text{R},0} + bQ_{\text{IR},0}^2)$, where a and b are negative coefficients in this case. The interpretation is that the oscillating IR phonon induces a change in the effective exchange constants because it appears as $Q_{\text{IR},0}^2$. That is, although the time average of Q_{IR} is zero—the average amplitude does not change—the time average of Q_{IR}^2 is not zero. This is essentially the same physics that produces the unidirectional displacement of the Raman phonons, since the IR mode also

appears as Q_{IR}^2 in the relevant coupling term in Eqs. (1) and (4). This effect of the IR phonon on magnetism has not been addressed previously in the nonlinear phononics literature; however, our results suggest that coupling between the spins and IR phonons cannot be ignored.

Figure 4 shows that although the system approaches the A-AFM state with increasing peak electric field, the FM state remains stable over the entire electric field range. The magnetic transition could be induced by simply increasing the peak electric field; however, it is desirable to keep the peak electric field as low as possible, in order to minimize sample damage and heating. We therefore need some way to position GdTiO_3 closer to the FM-A-AFM phase boundary.

Recent work has shown how strain engineering can tune $\text{La}_{(2/3)}\text{Ca}_{(1/3)}\text{MnO}_3$ into a charge-ordered insulating phase with extreme photo-susceptibility.¹³ Ultrafast optical excitation of the strained material induces a transition to a long-lived, hidden metallic phase. Likewise, we calculated the energy difference between the A-AFM, G-AFM, C-AFM, and FM states as a function of both tensile and compressive biaxial strain (the strain was applied in the plane perpendicular to the c -axis). Figure 5a shows that both tensile and compressive strain decrease the energy of all of the AFM phases relative to the FM state; however, the A-AFM phase again remains closest in energy to the FM state. In fact, epitaxial strain by itself can induce the A-AFM phase in GdTiO_3 . However, the strains required (tensile strains greater than 2% and compressive strains greater than 2.5%) are quite large and likely unrealizable in real GdTiO_3 thin films. Nonetheless, calculation of the relevant exchange coefficients and magnetic T_c does show how strain moves GdTiO_3 closer to the FM-A-AFM phase boundary. The difference between the FM and A-AFM phases corresponds to a change from FM to AFM ordering along the c -axis of the crystal. The out-of-plane exchange coefficient (J_c) tracks this energy difference well, as Fig. 5b shows. As the in-plane lattice constants increase, the in-plane (ab -plane) exchange coefficients (J_{ab}) decrease. This leads to a steady decrease in the critical T_c for tensile strain (Fig. 5c). Because of the sharp decrease in the out-of-plane exchange coefficient (J_c) with tensile strain we look for optically induced magnetic switching at $+1.5\%$ tensile strain, where the critical temperature is still large and J_{ab} is still greater than zero ($+1.5\%$ tensile strain corresponds approximately to growth on GdScO_3).^{7,28} Previous theoretical work has also explored strain as a possible strategy for stabilizing the A-AFM phase in rare earth titanates (and specifically GdTiO_3) although much larger values of strain were typically required.^{29–32}

Figure 6a now shows that excitation of the same IR-active phonon (now at 70.8 meV in the strained material) pushes GdTiO_3 across the phase boundary, stabilizing the A-AFM phase at lower peak electric fields than in the unstrained system. We find that the combined peak IR and Raman response stabilizes the A-AFM phase for $E_0 > 2.5 \text{ MV/cm}$. The average unidirectional Raman response alone requires $E_0 > 4.5 \text{ MV/cm}$ to induce this change, a still modest peak electric field value. These results suggest that a previously experimentally unidentified magnetic phase of the rare earth titanates may be reached dynamically by the nonlinear phononics process.

What is the structural origin of the switch from the FM to the A-AFM phase? To answer this question, we use the symmetry-adapted modes of the parent cubic $Pm\bar{3}m$ phase as a basis to decompose the non-equilibrium structural changes into contributions from different distortions (see Supplementary Information). Because the Raman displacement is quasi-static, we focus on this aspect of the structural changes. We group the components of the Raman modes into three categories, which have been highlighted in the titanate literature because of their effect on electronic and magnetic properties in the equilibrium phase diagram: two octahedral rotation distortions (transforming like the irreducible representations R_4^+ , for the $a^-a^-c^0$ rotation in Glazer notation, and

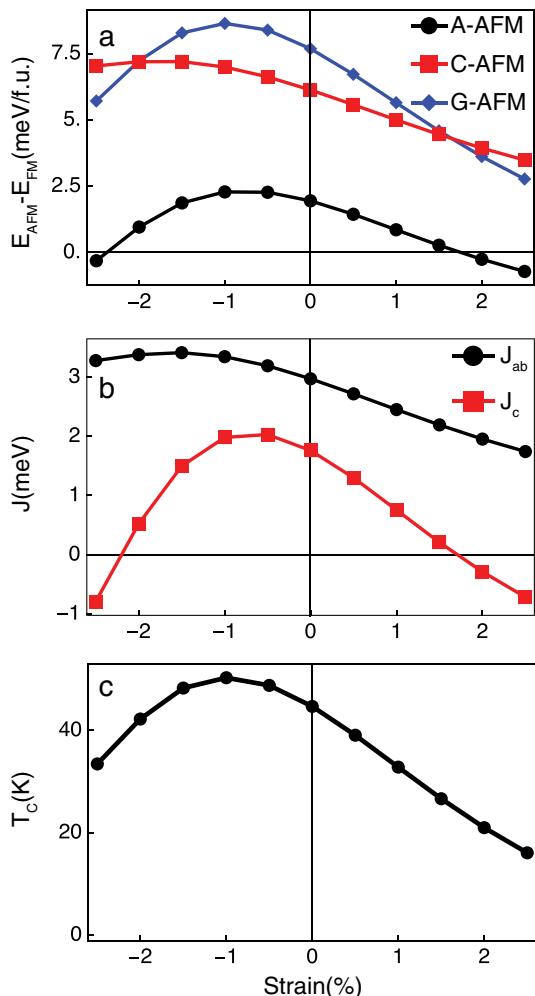


Fig. 5 Effect of epitaxial strain on magnetism in GdTiO_3 . **a** Magnetic configuration energy differences relative to the FM state. Again, positive energy differences indicate that the FM state is more stable than a particular AFM phase. Negative strains correspond to the compressive region, whereas positive strains are tensile. **b** In-plane (J_{ab}) and out-of-plane (J_c) Heisenberg exchange parameters ($J > 0$ corresponds to FM order) and **c** Weiss mean field critical temperature as a function of in-plane strain

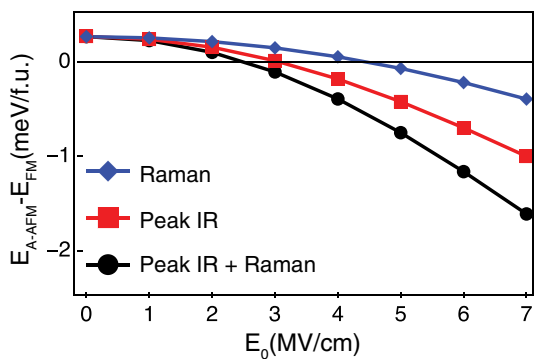


Fig. 6 Phonon-induced change in magnetism in +1.5% strained GdTiO₃. Simulated energy difference between the A-AFM and FM phases as a function of peak electric field for 70.8 meV, [001] polarized, IR phonon. This mechanism now stabilizes the A-AFM phase at experimentally realizable peak electric fields

M_3^+ for the in-phase $a^0a^0c^+$ rotation), three distortions that change Ti-O bond lengths (R_5^+O , X_5^+O , and M_2^+O represent distortions of the octahedral oxygen environment) and modes involving displacements of the Gd cations (R_5^+Gd and X_5^+Gd). Each A_g phonon is a linear combination of all three kinds of structural distortion, although some modes may be dominated by a particular type of distortion.

The two most commonly discussed structural distortions in the perovskite literature are the out-of-phase R_4^+O and in-phase M_3^+O octahedral rotations. As the schematic phase diagrams in Fig. 7 show, the amplitudes of these distortions increase in moving from La to Y in the rare earth titanate series ATiO₃ (A = La, Nd, Sm, Gd, Y); there is a concomitant change in magnetic order from G-AFM in LaTiO₃ to FM in YTiO₃. This change in magnetic order is usually understood as a response to changes in the Ti-O-Ti bond angles (which are directly affected by the rotation amplitudes) and subsequent changes in the magnetic superexchange interactions. However, if we try to interpret our results in terms of this picture, we find something unexpected. First, let us consider our strain results and focus on small strains $\pm 1\%$ around the bulk value, the region that is most likely to be applicable to thin-film experiments. Figure 5a shows that small tensile strains favor the A-AFM phase, whereas small compressive strains further stabilize the FM ground state. Now, how does this compare with the correlation between rotation angles and magnetism in bulk? The schematic phase diagrams in Fig. 7 show that increasing the R_4^+ and M_3^+ rotation angles favors the FM phase, whereas decreasing them favors the AFM phase. However, Fig. 7 also shows that compressive strain changes the R_4^+ and M_3^+ rotation angles such that the system is pushed towards the AFM-FM phase boundary, whereas small tensile strains push the system further into the FM region (red shaded region). This is the opposite behavior to what we would expect based on the results in Fig. 5. Quite astonishingly, if we now consider the dynamical response (blue shaded region), we see that as the peak electric field increases, the R_4^+ angle changes in such a way that the system moves away from the AFM-FM phase boundary. Moreover, the change in rotation angle across the whole range of strains and peak electric fields is very small, barely more than 1°. Similar results hold for the M_3^+ rotation (Fig. 7b), where the change in rotation angle is even smaller. Clearly, considering only changes in rotation angles cannot explain the transition to A-AFM order under optical excitation in GdTiO₃. (The strain results are essentially a volume effect but we defer further discussions to a forthcoming publication so we can focus here on the dynamical response.)

If changes in rotation angles do not induce a change in magnetic order in GdTiO₃ through the nonlinear phononics mechanism, then which structural distortion is responsible? Fig. 8a

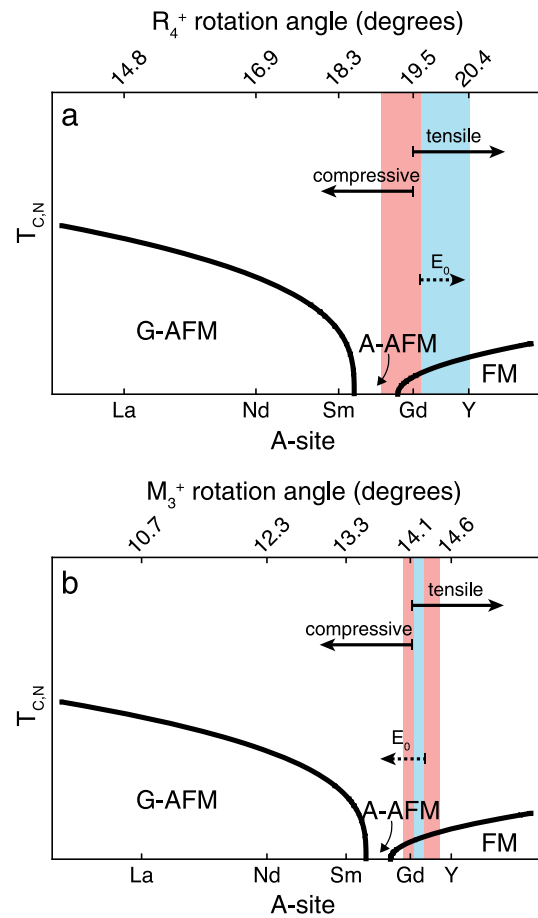


Fig. 7 Titanate magnetic phase diagram versus rotation angle. The **a** out-of-plane rotation (R_4^+) and **b** in-plane rotation angles (M_3^+) accessed by epitaxial strain (red) and the nonlinear phononics approach in +1.5% strained GdTiO₃ (blue) cannot account for the change in magnetism to the A-AFM phase. The lower horizontal axis shows the A-site while the upper horizontal axis shows a least squares fit to the rotation angle from the simulated structures in the corresponding magnetic phase. Phase boundaries have been drawn schematically with magnetic phases identified. The predicted A-AFM phase is shown in the purple region. Arrows showing the qualitative change in rotation angle have been included for the compressive/tensile strain (solid) and peak electric field E_0 (dashed)

shows the percentage change in the symmetry-adapted mode distortion amplitudes as a result of optical excitation (the same plot showing absolute changes can be found in the Supplementary Information). Positive changes indicate that the distortion increases in magnitude relative to the equilibrium structure, whereas negative changes indicate that the distortion decreases in magnitude. The M_2^+ Jahn-Teller mode undergoes the largest change by far, increasing in magnitude with respect to the equilibrium structure (this corresponds to a 158% change in the Jahn-Teller amplitude at a peak electric field of 7 MV/cm). The R_5^+ mode, which changes the O and Gd environments, also increases in magnitude. In contrast, the two octahedral rotation modes, R_4^+ and M_3^+ , change very little. Contrary to conventional wisdom, our results suggest that judicious tuning of octahedral rotation angles is unlikely to produce the desired A-AFM phase under experimentally realizable conditions. Instead, the Jahn-Teller mode is playing the key role in the magnetic switching process. To test this insight, we re-calculated the energy difference between the FM and A-AFM phases while selectively returning specific sets of distortions to their equilibrium values. Figure 8b shows that when all modes are returned to their

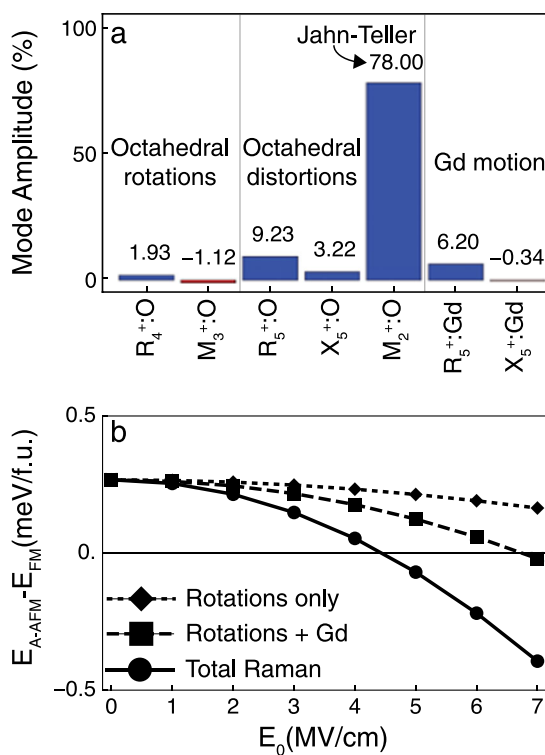


Fig. 8 Structural contributions to the magnetic phase change. **a** Percent change in the symmetry-adapted mode amplitude for the Raman component of the non-equilibrium strained GdTiO_3 structure. Blue (red) corresponds to an increase (decrease) in amplitude. Note that the percentages sum to 100%. **b** Nonlinear phononics change in the magnetic energy difference between the A-AFM and FM phases with octahedral rotations only (dashed), rotations and octahedral distortions (dotted), and total Raman response (solid)

equilibrium values except for the two rotation modes, the FM phase is stable over the entire range of peak electric fields we consider. When all modes are returned to their equilibrium values except the rotations and those involving displacements of the Gd ions, there is a crossover from the FM to the A-AFM phase at high peak electric fields. Inclusion of the M_2^{+} Jahn-Teller mode pushes the crossover to lower peak electric fields.

DISCUSSION

Our results demonstrate that the nonlinear phononics mechanism can be exploited to dynamically stabilize the A-AFM phase of GdTiO_3 in the manner suggested by Mochizuki and Imada—by modulating the amplitude of the Jahn-Teller mode while changing the rotations very little, a combination of conditions that is extremely difficult to realize in either bulk or thin-film GdTiO_3 . The “indirectness” of the nonlinear phononics process—light is used to excite a particular phonon mode, which then produces a displacement of another set of modes through anharmonic coupling—is sometimes seen as a disadvantage of the mechanism, since ions are only displaced from their equilibrium values by very small amounts. In this case, however, the indirect nature of the mechanism is probably precisely what allows the stabilization of the A-AFM phase. Octahedral rotations are very low-energy distortions, in that they lower the energy of the cubic perovskite phase by a significant amount (over 1 eV in some cases) and have very large amplitudes in the distorted Pbnm structure. Large amounts of energy, supplied through epitaxial strain, for example, are therefore required to change their

amplitudes. In contrast, the amplitude of the Jahn-Teller mode is typically orders of magnitude smaller. We speculate that the nonlinear phononics mechanism supplies just enough energy to induce changes in the Jahn-Teller mode in GdTiO_3 , but not enough to significantly affect the octahedral rotations. Of course, the dynamical response of other perovskites may be different; the structures of perovskites out of equilibrium are only beginning to be explored in detail, and so much more work is needed in this area.

There is some experimental support for our findings. Zhang et al.³³ grew very thin films of GdTiO_3 , such that the octahedral rotations are suppressed. However, they found that ferromagnetism persisted, even in the absence of rotation distortions, and posit that the magnetism is controlled by “the narrow bandwidth, exchange, and orbital ordering”. Regardless of the mechanism, clearly octahedral rotations are not as essential to the magnetic properties of GdTiO_3 as has perhaps been assumed. Experimental confirmation of the dynamical magnetic response can in principle be achieved by time-resolved Faraday or Kerr probes³⁴ referenced to the infrared lattice excitation, while corresponding birefringence measurements can detect changes in the Jahn-Teller mode amplitude.

We conclude by emphasizing that we are emphatically not claiming that octahedral rotations are never important in giving rise to the electronic and magnetic properties of perovskites. There is a large and well-established theoretical and experimental literature unambiguously showing the various ways in which these distortions affect the properties of perovskites. However, in the case of the rare earth titanates at least, it appears that octahedral rotations merely “set the stage” for the magnetic properties, while much smaller structural distortions (such as the Jahn-Teller mode) work together to induce the actual magnetic ground state.

METHODS

First-principles calculations

First-principles calculations were performed using projector augmented wave potentials and the PBEsol+U exchange-correlation functional, as implemented in VASP. On-site Coulomb and exchange parameters of $U_{\text{Ti},d} = 5$ eV, and $J_{\text{Ti},d} = 0.64$ eV were used³⁵ (we found no qualitative change in our results for reasonable variations of U). We use a 600 eV plane wave cut-off and a $6 \times 6 \times 4$ Monkhorst-Pack grid. These choices produced good agreement with available experimental structural data for ATiO_3 (A = La, Nd, Sm, Gd, Y)³⁶ (see Supplementary Fig. 3 for detailed comparison of GdTiO_3). For GdTiO_3 we find the lattice constants $a = 5.372 \text{ \AA}$, $b = 5.768 \text{ \AA}$, $c = 7.646 \text{ \AA}$, in good agreement with available high-temperature experimental values $a = 5.393 \text{ \AA}$, $b = 5.691 \text{ \AA}$, $c = 7.664 \text{ \AA}$. Phonons and Born charges were calculated using density functional perturbation theory within VASP and used to calculate dynamical mode effective charges (\tilde{Z}_i^*) and to model the frequency-dependent dielectric response³⁷.

Magnetic exchange and critical temperature

Magnetic exchange constants were calculated by fitting the A-, C-, G-AFM, and FM configuration energies to a Heisenberg model $E_{\text{magnetic}} = - \sum_{\langle i,j \rangle_y} J_y \mathbf{S}_i \cdot \mathbf{S}_j$, where $\langle i,j \rangle_y$ labels nearest neighbors for in-

plane ($y = ab$) and out-of-plane ($y = c$) spins. We note that including both Raman and IR phonons in the Heisenberg model results in an effective exchange coupling $J_y \rightarrow J_y \left(1 + a_y Q_{\text{R},0} + b_y Q_{\text{IR},0}^2 \right)$, with both $a_y Q_{\text{R},0}$ and $b_y Q_{\text{IR},0}^2$ reaching negative values, inducing the FM to A-AFM phase transition. Here $Q_{\text{IR},0}$ is the excited IR phonon and $Q_{\text{R},0}$ is the total induced Raman distortion—see Fig. 8a.) The critical temperature T_C is evaluated from the spin-1/2 molecular field theory result with total exchange field of $4J_a b + 2J_c$ per spin.

Strain response of GdTiO_3

Strain was considered for both common growth modes of Pbnm perovskites. The first corresponds to growth along the c -axis and maintains

REFERENCES

1. Hwang, H. Y., Cheong, S., Radaelli, P. G., Marezio, M. & Batlogg, B. Lattice effects on the magnetoresistance in doped LaMnO₃. *Phys. Rev. Lett.* **75**, 914–917 (1995).
2. Medarde, M. L. Structural, magnetic and electronic properties of RNiO₃ perovskites (R = rare earth). *J. Phys. Condens. Matter* **9**, 1679–1707 (1997).
3. Zhou, J. & Goodenough, J. B. Chemical bonding and electronic structure of RNiO₃ (R = rare earth). *Phys. Rev. B* **69**, 153105 (2004).
4. Catalan, G. Progress in perovskite nickelate research. *Phase Transit.* **81**, 729–749 (2008).
5. Mochizuki, M. & Imada, M. Orbital physics in the perovskite Ti oxides. *New. J. Phys.* **6**, 154 (2004).
6. Pavarini, E. et al. Mott transition and suppression of orbital fluctuations in orthorhombic 3d¹ perovskites. *Phys. Rev. Lett.* **92**, 176403 (2004).
7. Choi, K. J. et al. Enhancement of ferroelectricity in strained BaTiO₃ thin films. *Science* **306**, 1005–1009 (2004).
8. Lee, J. H. et al. A strong ferroelectric-ferromagnet created by means of spin-lattice coupling. *Nature* **466**, 954–958 (2010).
9. Kim, T. H. et al. Polar metals by geometric design. *Nature* **533**, 68–71 (2016).
10. Hiroi, Z., Takano, M., Azuma, M. & Takeda, Y. A new family of copper oxide superconductors Sr_{n+1}Cu_nO_{2n} stabilized at high pressure. *Nature* **364**, 315–317 (1993).
11. Miyano, K., Tanaka, T., Tomioka, Y. & Tokura, Y. Photoinduced insulator-to-metal transition in a perovskite manganite. *Phys. Rev. Lett.* **78**, 4257–4260 (1997).
12. Kiryukhin, V. et al. An x-ray-induced insulator-metal transition in a magnetoresistive manganite. *Nature* **386**, 813–815 (1997).
13. Zhang, J. et al. Cooperative photoinduced metastable phase control in strained manganite films. *Nat. Mater.* **15**, 956–960 (2016).
14. Rini, M. et al. Control of the electronic phase of a manganite by mode-selective vibrational excitation. *Nature* **449**, 72–74 (2007).
15. Subedi, A., Cavalleri, A. & Georges, A. Theory of nonlinear phononics for coherent light control of solids. *Phys. Rev. B* **89**, 220301(R) (2014).
16. Tomioka, Y., Asamitsu, A., Kuwahara, H., Moritomo, Y. & Tokura, Y. Magnetic-field-induced metal-insulator phenomena in Pr_{1-x}Ca_xMnO₃ with controlled charge-ordering instability. *Phys. Rev. B* **53**, R1689–R1692 (1996).
17. Tokura, Y. Critical features of colossal magnetoresistive manganites. *Rep. Prog. Phys.* **69**, 797 (2006).
18. Tobey, R. I., Prabhakaran, D., Boothroyd, A. T. & Cavalleri, A. Ultrafast electronic phase transition in La_{1/2}Sr_{3/2}MnO₄ by coherent vibrational excitation: evidence for nonthermal melting of orbital order. *Phys. Rev. Lett.* **101**, 197404 (2008).
19. Mankowsky, R. et al. Nonlinear lattice dynamics as a basis for enhanced superconductivity in YBa₂Cu₃O_{6.5}. *Nature* **516**, 71–73 (2014).
20. Subedi, A. Proposal for ultrafast switching of ferroelectrics using midinfrared pulses. *Phys. Rev. B* **92**, 214303 (2015).
21. Fechner, M. & Spaldin, N. A. Effects of intense optical phonon pumping on the structure and electronic properties of yttrium barium copper oxide. *Phys. Rev. B* **94**, 134307 (2016).
22. Juraschek, D., Fechner, M. & Spaldin, N. A. Ultrafast structure switching through nonlinear phononics. *Phys. Rev. Lett.* **118**, 054101 (2017).
23. Pavarini, E., Yamasaki, A., Nuss, J. & Andersen, O. K. How chemistry controls electron localization in 3d¹ perovskites: a Wannier function study. *New. J. Phys.* **7**, 188 (2005).
24. Först, M. et al. Nonlinear phononics as an ultrafast route to lattice control. *Nat. Phys.* **7**, 854–856 (2011).
25. Zhao, X. & Vanderbilt, D. Phonons and lattice dielectric properties of zirconia. *Phys. Rev. B* **65**, 075105 (2002).
26. Gonze, X. & Lee, C. Dynamical matrices, born effective charges, dielectric permittivity tensors, and interatomic force constants from density-functional perturbation theory. *Phys. Rev. B* **55**, 10355–10368 (1997).
27. Nova, T. F. et al. An effective magnetic field from optically driven phonons. *Nat. Phys.* **13**, 132 (2017).
28. Uecker, R. et al. Spiral formation during Czochralski growth of rare-earth scandates. *J. Cryst. Growth* **295**, 84–91 (2006).
29. Huang, X., Tang, Y. & Dong, S. Strain-engineered A-type antiferromagnetic order in YTiO₃: a first-principles calculation. *J. Appl. Phys.* **113**, 17E108 (2013).
30. Weng, Y., Huang, X., Tang, Y. & Dong, S. Magnetic orders of LaTiO₃ under epitaxial strain: a first-principles study. *J. Appl. Phys.* **115**, 17E108 (2014).
31. Yang, L.-J., Weng, Y.-K., Zhang, H.-M. & Dong, S. Strain driven sequential magnetic transitions in strained GdTiO₃ on compressive substrates: a first-principles study. *J. Phys. Condens. Matter* **26**, 476001 (2014).
32. Huang, X., Xu, Q. & Dong, S. Orientation-dependent magnetism and orbital structure of strained YTiO₃ films on LaAlO₃ substrates. *J. Appl. Phys.* **117**, 17C703 (2015).

the *Pbnm* space group (# 62). The second corresponds to growth perpendicular to the *c*-axis. This lowers the symmetry to *P2₁/m* (#11). We find that for tensile strain on orthorhombic substrates, the *Pbnm* phase is generally preferred. In the specific case addressed in the main text, +1.5% strain corresponds approximately to growth on GdScO₃.

Calculation of non-equilibrium force constants

To calculate the non-equilibrium force constants, we use a finite-difference approach where force constant matrices (Φ) are calculated for each A_g phonon, displaced about equilibrium. The non-equilibrium force constant matrices are then used to calculate the nonlinear coupling coefficients between the A_g and the IR phonons ($A_{i\alpha\alpha}$, $B_{ij\alpha\beta}$, $C_{\alpha\beta\gamma\beta}$) by projecting the force constant matrices into the basis of the equilibrium structure. For example, the real-space coupling between A_g Raman mode a , and IR modes i and j is found by $(\Phi_i(u_a) - \Phi_j(-u_a))/2u_a$. Here, u_a is the real-space eigendisplacement amplitude associated with phonon Q_a . In *Pbnm* this approach requires 15 phonon calculations: 1 for the equilibrium structure, and two increments for each of the 7 A_g modes. All third-order terms that couple to Q_a are found in this way. We therefore have all necessary third-order coupling terms for the nonlinear phononics process. This approach is significantly less computationally burdensome than finite-difference techniques that calculate all third-order terms, or frozen-phonon techniques that require converged meshes in phonon amplitude. In *Pbnm* the frozen-phonon technique would require 175 two-dimensional meshes to calculate $A_{i\alpha\alpha}$, 651 three-dimensional meshes to calculate $B_{ij\alpha\beta}$ and 84 three-dimensional meshes to calculate all $C_{\alpha\beta\gamma\beta}$. Regardless, we have tested our computational approach against the frozen-phonon method for multiple randomly selected $A_{i\alpha\alpha}$, $B_{ij\alpha\beta}$ and $C_{\alpha\beta\gamma\beta}$ and found good agreement. We note that this computational technique may also be used for coupling to non- A_g Raman modes. In that case u_a labels the real-space eigendisplacement amplitude of the non- A_g mode of interest.

Optical pulse characteristics

Phonon frequencies, dynamical mode effective charges, nonlinear coupling coefficients, and optical pulse characteristics are fed into Eqs. (5) and (6), which are numerically simulated to find the dynamical response. We include all IR phonons polarized parallel to the incident light as well as all A_g phonons in our simulations. We fix the timescale τ (full-width at half-maximum) of a Gaussian pulse to be 300 fs and vary the peak electric field (E_0) from 1 to 7 MV/cm for carrier frequencies on resonance with the desired IR phonon (for a Gaussian pulse the extrinsic quantity $(E_0\tau)^2$ affects the Raman subspace; the electric field range has been chosen consistent with experimentally reported values.^{14,38}

Data availability

Data are available upon reasonable request from the corresponding author.

ACKNOWLEDGEMENTS

This work was supported by the National Science Foundation. N.A.B. was supported by DMR-1550347. Initial work on this project by G.K. was supported by DMR-1550347, and subsequently by the Cornell Center for Materials Research with funding from the National Science Foundation MRSEC program (DMR-1719875). This work used the Extreme Science and Engineering Discovery Environment (XSEDE) (through allocation DMR-160052), which is supported by National Science Foundation grant number ACI-1548562. We thank Farhan Rana, Jeffrey Moses, Craig Fennie and Gregory Fuchs for helpful discussions.

AUTHOR CONTRIBUTIONS

The authors contributed equally to this work.

ADDITIONAL INFORMATION

Supplementary information accompanies the paper on the *npj Quantum Materials* website (<https://doi.org/10.1038/s41535-018-0086-3>).

Competing interests: The authors declare no competing interests.

Publisher's note: Springer Nature remains neutral with regard to jurisdictional claims in published maps and institutional affiliations.

33. Zhang, J. Y., Jackson, C. A., Raghavan, S., Hwang, J. & Stemmer, S. Magnetism and local structure in low-dimensional Mott insulating GdTiO_3 . *Phys. Rev. B* **88**, 121104 (R) (2013).
34. Kampfrath, T. et al. Coherent terahertz control of antiferromagnetic spin waves. *Nat. Photon.* **5**, 31–34 (2011).
35. Okamoto, S., Millis, A. J. & Spaldin, N. A. Lattice relaxation in oxide heterostructures: $\text{LaTiO}_3/\text{SrTiO}_3$ superlattices. *Phys. Rev. Lett.* **97**, 056802 (2006).
36. MacLean, D. A., Ng, H.-N. & Greedan, J. E. Crystal structures and crystal chemistry of the RETiO_3 perovskites: $\text{RE} = \text{La, Nd, Sm, Gd, Y}$. *J. Solid State Chem.* **30**, 35–44 (1979).
37. Gonze, X. & Lee, C. Dynamical matrices, born effective charges, dielectric permittivity tensors, and interatomic force constants from density-functional perturbation theory. *Phys. Rev. B* **55**, 10355–10368 (1997).
38. Mankowsky, R., von Hoegen, A., Först, M. & Cavalleri, A. Ultrafast reversal of the ferroelectric polarization. *Phys. Rev. Lett.* **118**, 197601 (2017).



Open Access This article is licensed under a Creative Commons Attribution 4.0 International License, which permits use, sharing, adaptation, distribution and reproduction in any medium or format, as long as you give appropriate credit to the original author(s) and the source, provide a link to the Creative Commons license, and indicate if changes were made. The images or other third party material in this article are included in the article's Creative Commons license, unless indicated otherwise in a credit line to the material. If material is not included in the article's Creative Commons license and your intended use is not permitted by statutory regulation or exceeds the permitted use, you will need to obtain permission directly from the copyright holder. To view a copy of this license, visit <http://creativecommons.org/licenses/by/4.0/>.

© The Author(s) 2018